

# Initial formation of channels and shoals in a short tidal embayment

By **H. M. SCHUTTELAARS**<sup>1</sup>† AND **H. E. de SWART**<sup>2</sup>

<sup>1</sup>Mathematical Institute, Utrecht University, P.O.Box 80.010, 3508 TA Utrecht, The Netherlands

<sup>2</sup>Institute for Marine and Atmospheric Research, Utrecht University, P.O.Box 80.000, 3508 TA Utrecht, The Netherlands

(Received 15 May 1997)

It is demonstrated by using a simple model, that bedforms in a short tidal embayment can develop due to a positive feedback between tidal currents, sediment transport and bedforms. The system is forced by a prescribed free surface elevations at the entrance of the embayment. The water motions are modelled by the depth-integrated shallow water equations. For the sediment dynamics a diffusively dominated suspended load transport model is considered. Tidal averaging is used to obtain the bottom profiles at the long morphological time scale.

The stability of the linearly sloping equilibrium bottom profile is studied for various combinations of the model parameters. It turns out that without a mechanism that generates vorticity the equilibrium profile is stable. In that case small-scale perturbations can at most become marginally stable if no slope correction term in the bottom evolution equation is added. If vorticity is generated in our model by bottom friction torques, the basic state is unstable. Which modes are unstable and what their growth rate is depends among others on the strength of the bottom friction, the width of the embayment and the grain size: if the sediment under consideration consists of large particles, the equilibrium will be more stable than when smaller particles are considered. Without a diffusive term in the bed evolution equation, small scale perturbations become unstable. To avoid this physically unrealistic behaviour slope correction terms are included in the sediment transport. Furthermore, it is shown that using an asymptotic expansion for the concentration as given in earlier literature is only valid for small or moderate mode numbers and the technique is extended to large mode numbers. A physical interpretation of these results is also given.

---

† This research was supported by NWO-grant nr. NLS 61-261 and by the EU-sponsored Marine Science and Technology Programme (MAST-III), under contract no. MAS3-CT95-0002 (PACE project). Furthermore, we thank A. van Harten and A. Doelman for their comments on earlier versions of this paper.

## 1. Introduction

In most tidal embayments a delicate balance between large in – and outgoing fluxes exists. During the flood period large amounts of sediment are transported into the embayment, while during the ebb period a large amount of sediment leaves the embayment again. Due to erosion and deposition during the tidal cycle, the bottom evolves and usually organizes itself in a pattern of shallow shoals separated by deep channels (see e.g. [10]). The channel system often exhibits a fractal-like structure with the number of channels increasing and their depth decreasing in the land ward direction. The channel–shoal systems are very important from both an ecological point of view as well as from an economical viewpoint. Since the balance in these tidal embayments is very sensitive for external factors [15], the equilibrium in these regions can be easily disturbed. A well-studied example is the Frisian inlet system: in 1969 a part of its channel–shoal system (the Lauwers Sea) was closed with a dam. This reduced the tidal prism (the embayment volume between high and low water mark) of the system with 30% [16] and its dynamic equilibrium was disturbed. The inlet system started to change by shoaling of the tidal channels, eroding the deeper parts of the outer delta and forming large bars. In this system, cyclic bar behavior was observed before the closure of the Lauwers Sea [16]. In one of the major channels of the Frisian Inlet system, the Pinkegat Inlet, this cyclic behavior is still observed after the closure, in the other major inlet, the Zoutkamperlaag Inlet, this cyclic behavior stopped. This indicates that the system is adjusting to another equilibrium.

The mathematical–physical modeling of the interaction between water motion and the erodeable bottom is a rapidly developing field of research. Originally most models were of empirical or semi–empirical type, see e.g. [25] and the review [6]. These models are (partly) based on statistical relationships between different state variables (e.g. that between the cross–sectional area and the tidal prism) which were derived from analyzing field data. At a later stage process–oriented models were developed which are based on physical principles. The first studies with such models focused on the dynamics of currents induced by tides without any feedback to morphology [2, 24, 7, 17, 13]. The last few years the morphodynamics of tidal inlets and basins has received more attention, see the review [5]. In [29, 28] a numerical model was developed with which they were able to simulate present–day morphological behavior of the Frisian Inlet and its response to the closure of the Lauwers Sea. A similar, but simpler model (based on time–integration of tidally averaged equations, see below) was developed in [4] and applied to the Western Scheldt Estuary. Unfortunately, these models are too complex to determine the basic mechanisms responsible for the behavior of the simulated phenomena.

This was the motivation for the study as reported in [22], where an idealized one–dimensional morphologic model of a short tidal embayment with a constant width was considered. It was demonstrated that for realistic parameter values this system has one morphodynamic equilibrium which is reached for arbitrary initial conditions. The bottom profile in this final state depends on the parameter values selected and is such that in the embayment a spatially uniform shear stress distribution is attained, which seems to be consistent with field observations [12]. Moreover, the relation between cross–sectional area and the tidal prism appears to be linear as data indicate [6]. Finally, the model predicts a net import of sediment if its length is suddenly reduced, which is consistent with the behavior of the Frisian Inlet. However, a serious limitation of this model is that it cannot explain the high morphologic activity observed in natural tidal basins.

In this paper, it will be shown that the formation of channels and shoals may be due to an inherent positive feedback between tidal currents and the erodeable bed. This will

be done by investigating the stability properties of the equilibrium state of the model as discussed in [22] within the context of a two-dimensional model. The motivation for this approach comes from studies in river dynamics in which it was found that the use of a two-dimensional model is a necessary condition for obtaining morphologic instabilities (see [20] and references herein). This stability concept is also used in [23], but an important difference with the present study is that they consider the estuary as an open tidal river, and that our model is depth integrated. However, we believe that our simplified two dimensional model contains enough physics to give some insight in the origin of the channel-shoal systems and behavior as observed in these systems, *i.e.* cyclic bar behavior as observed in the Frisian inlet system [16].

The paper is organized as follows. In section 2 the model equations and boundary conditions are introduced. The embayment under consideration is rectangular with only the bottom erodeable. Its length is considered to be small compared to the tidal wave length such that the system is far from resonance (this condition is marginally obeyed by, for example, the Frisian inlet system). Depth averaged shallow water equations are used to describe the water motion. The sediment transport model considered consists only of diffusive suspended load transport. Introducing advective transport will only complicate the equations. The only bedload transport term incorporated is the bedslope effect which accounts for the tendency of sediment to move easier downslope and uphill. Since morphological time scales are much larger than tidal time scales, the method of averaging [19] can be used, meaning that effectively hydrodynamics and morphodynamics are decoupled. In section 3, the embayment is tidally forced by the leading order tidal constituent at the entrance of the basin. An equilibrium state of the equations is found which is spatially uniform in the lateral direction. This implies that it is also a solution of the corresponding one-dimensional model. In section 4 the stability of this equilibrium is investigated. The concentration equation is solved exactly using numerical tools. This is in contrast with [22] where an asymptotic approximation of the concentration was used. Using an irrotational velocity field two-dimensional perturbations are studied. By allowing no variation in the lateral direction one-dimensional perturbations are obtained. These results are compared with [22]. Furthermore, the effect of a small bedload term is studied. It turns out that for large mode numbers in the lateral direction the complete concentration equation has to be solved since the approximation as used in [22] is only correct for low mode numbers. Furthermore, stability results are given and the physical mechanism is discussed. It turns out that without vorticity, the equilibrium profiles are stable. Therefore, another, more realistic parameterization of the friction terms is introduced in the momentum equations. With this parameterization two dimensional perturbations can become linearly unstable. A preferred mode and critical conditions are found (this instability and preferred mode were observed in complex morphodynamic model called DELFT2D-MOR as well). Plots of the velocity fields, concentration and bottom profiles and sediment fluxes are presented to clarify the physical mechanism behind this instability. In the last section, the results are recapitulated and discussed in the context of field observations. Moreover, some suggestions for further investigations are made.

## 2. Model Description

The geometry which will be considered is that of an idealized tidal embayment of rectangular shape (width  $B$  and length  $L$ ), ignoring width variations that often strongly constrain the dynamics [13]. The coast-lines are assumed to be fixed whereas the bottom (described by  $z = -H + h$ , with  $H$  a reference depth) is erodeable. The free surface is

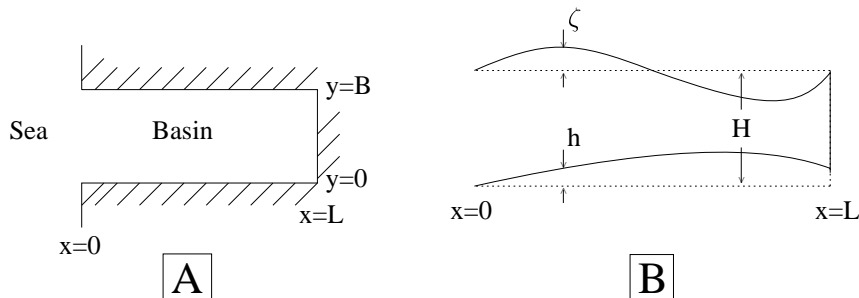


FIGURE 1. Situation sketch: top view [A] and cross-sectional view [B] of the tidal embayment.

described by  $z = \zeta$  (see figure 1). The hydrodynamic part of the equations is described by the depth-averaged shallow water equations for a homogeneous fluid [3, 27]. This set of equations is supplemented with a depth-averaged concentration equation [26] which describes sediment fluxes due to both advective and diffusive processes and the bottom evolution equation. The bottom evolves both due to transport of suspended sediment and bedload transport [8, 26]. As boundary conditions the free surface elevation at the entrance of the basin is prescribed (including tidal motions with a characteristic frequency  $\sigma$ ) and we require that there is no normal water and sediment transport at solid boundaries.

The equations that describe the morphodynamics of the tidal embayment as discussed in this paper are given below in dimensionless form (for a derivation of the unscaled equations, see [27]; for details, see [22]). Here we consider a short embayment, *i.e.*, its length is much smaller than the tidal wave-length  $L_g = \sqrt{gH}/\sigma$ . Moreover, earth rotation effects and advective terms will be neglected in the equations of motion. These assumptions can only be justified for a limited number of natural embayments, see the discussion at the end of this section. However, it is worthwhile to remark that they are not necessary conditions for the general applicability of the forthcoming analysis. They are merely introduced to make this analysis as transparent as possible without excluding the essential mechanisms. The simplified continuity equation is given by

$$\zeta_t + [(1-h)u]_x + [(1-h)v]_y = 0 \quad (2.1)$$

and the momentum equations and the vorticity equation by

$$\zeta_x = 0 \quad (2.2a)$$

$$\zeta_y = 0 \quad (2.2b)$$

$$v_{xt} - u_{yt} = -F_{2x}^b + F_{1y}^b \quad (2.2c)$$

with  $\mathbf{F}^b$  the dimensionless bottom friction vector. Note that the momentum equations describe a spatially uniform free surface, which is the consequence of the assumption of a short embayment. First, the dimensional friction vector is considered, defined as

$$\mathbf{F}_*^b = -\frac{\boldsymbol{\tau}_*^b/\rho}{H-h+\zeta}$$

with  $\boldsymbol{\tau}_*^b$  the stresses due to bottom friction. From observations and dimension analysis it follows that a suitable parameterization for the bed shear stress is the quadratic friction

law. However, our main objective is not to give a detailed description of the tidal flow but rather study its gross features. Therefore we adopt a linear friction law which reads in dimensional units

$$\boldsymbol{\tau}_*^b = \rho r_* \mathbf{u} \quad (2.3)$$

with  $\rho$  the density and  $r_*$  a friction parameter with dimensions  $ms^{-1}$ . This parameterization avoids the complications which result from the application of a quadratic friction law, without neglecting the essential physics of the problem. The parameter  $r_*$  is chosen such that the net dissipation of energy (averaged over the tidal cycle and embayment) due to the linearized shear stress (2.3) equals that of the bed shear stress based on the quadratic friction law. More details on this procedure are given in [30, 31]. It implies that  $r_*$  is proportional to the tidal current amplitude  $U$  and the bottom roughness. This will be used later on in this paper. Typical values for  $r_*$  in tidal embayments are  $\mathcal{O}(10^{-3}ms^{-1})$ .

Unfortunately, all parameterizations of the bottom stress vector have the property that friction terms become unbounded if the water depth tends to zero, unless the shear stresses scale at least linearly with the water depth in this limit. Since the frictional term should stay finite even as  $h \rightarrow 1$ , in order to have bounded solutions, the following parameterization (in dimensionless form) is used:

$$\mathbf{F}_b = r \mathbf{u} (1 + \alpha h + \dots) \quad (2.4)$$

where  $\alpha$  is an order parameter and  $r = r_*/(H\sigma)$  a dimensionless coefficient. Characteristic values for  $r$  are  $\mathcal{O}(0.1-1)$ . If  $\alpha = 0$ , vorticity is conserved, if  $\alpha \neq 0$  a mechanism to generate and dissipate vorticity is introduced. Formally  $\alpha$  should have a value of 1. In the following, only the first term of the Taylor expansion is taken into account.

The concentration equation reads

$$aC_t = (u^2 + v^2) - C + a\mu[C_{xx} + C_{yy}], \quad (2.5)$$

with  $a = \sigma/\gamma$ , the product of the e-folding time scale related to the deposition process,  $\gamma^{-1}$ , and the tidal period  $\sigma$ . Typical values of  $a$  are  $\mathcal{O}(10^{-1} - 10^{-3})$ . The non dimensional horizontal sediment diffusion coefficient is denoted by  $\mu$  with typical values of  $\mathcal{O}(10^{-2} - 10^{-3})$ . Both from field observations [9] and theoretical considerations it is known that the erosion term will be some power of the absolute velocity. Here we choose (in dimensional units) a quadratic parameterization (in accordance with field observations):

$$\text{Erosion} = \eta (u^2 + v^2)$$

where  $\eta$  ( $\mathcal{O}(10^{-4}kg\,m^{-2}\,s^{-1})$ ) is an erosion constant which depends on the sediment characteristics. At this point it is useful to remark that choosing any other exponent ( $\geq 1$ ) of the absolute velocity would yield qualitatively similar results. The deposition term is proportional to the sediment concentration. The bottom evolution equation is given by

$$h_\tau = - \langle (u^2 + v^2) - C \rangle + \lambda \langle \nabla^2 (h - h_{eq}) \rangle \quad (2.6)$$

Here  $h_{eq}$  is an as yet unspecified equilibrium profile of the equations,  $\tau = \delta_s t$ , with  $\delta_s = T/T_s$ , where  $T$  is the tidal period and  $T_s$  is the time scale related to suspended load, depending on sediment properties, tidal amplitude and water depth, and  $\langle \cdot \rangle$  denotes averaging over the tidal period. This formulation is based on the assumption that in natural embayments  $\delta_s \ll 1$ . Consequently, the bottom variable  $h$  may be considered stationary on the short tidal time scale and its evolution is only determined by the net

sediment transports averaged over a tidal cycle. The mathematical foundations of this approach are discussed in [19, 14]. In the systems under study, suspended load transport is orders of magnitude larger than bedload transport (see table 1, where  $\delta_b = T/T_b$ , with  $T_b$  the time scale related to bedload transport). Therefore, bedload transport can be neglected, apart from the gravitational term which is necessary to stabilize fast oscillating modes. The magnitude of this term is denoted by  $\lambda$ , which is a small parameter ( $\mathcal{O}(10^{-7} - 10^{-6})$ ). Note that the bedload term in (2.6) only gives a contribution if the bottom is perturbed from an equilibrium  $h_{\text{eq}}$ . This means that in morphodynamic equilibrium there is no bedload transport due to bottom slopes (effect compensated by transports due to waves). However, if the system is perturbed, bottom fluxes give a (small) contribution (see [11]).

The boundary conditions at the fixed coast lines are given by

$$(1-h)\mathbf{u} \cdot \mathbf{n} = 0, \quad \mu \nabla C \cdot \mathbf{n} = 0, \quad \lambda \nabla (h - h_{\text{eq}}) \cdot \mathbf{n} = 0 \quad \text{at } x = 1, y = 0, y = \frac{B}{L} \quad (2.7)$$

where  $\mathbf{n}$  is the normal vector. They require the normal fluxes of water and sediment to vanish at these locations. At the open boundary, the conditions read

$$\zeta = T(t), \quad S = 0, \quad h_\tau = 0 \quad \text{at } x = 0 \quad (2.8)$$

with  $S = (u^2 + v^2) - C$ . Here  $T(t)$  is a prescribed forcing of tidal origin which drives the water motions in the embayment. Note that there are no spatial shifts in the free surface elevation across the entrance. Hence it is a priori assumed that the width of the embayment is much smaller than the tidal wave-length. The two other conditions imply a balance between erosion and deposition and a fixed bottom at this location.

The equations were made dimensionless by using the following scaling (note that with this scaling  $0 \leq y \leq B/L$ ):

$$\begin{aligned} x &= Lx^* & y &= Ly^* & u &= Uu^* & v &= Uv^* \\ h &= Hh^* & t &= \sigma^{-1}t^* & \zeta &= \frac{HU}{\sigma L}\zeta^* & C &= \frac{\alpha U^2}{\gamma}C^*. \end{aligned} \quad (2.9)$$

For a motivation of this scaling, see [22]. Here  $U$  is the characteristic velocity scale in the longitudinal direction, related to the tidal forcing (with frequency  $\sigma$ ) at the entrance of the embayment. The coefficient  $\alpha$  is related to sediment properties (grain size, shape, etc.), with typical values  $\mathcal{O}(10^{-2} - 10^{-4} \text{kgsm}^{-4})$  corresponding to fine and medium sand, respectively. Note that the dimensionless horizontal diffusion coefficient  $\mu$  is defined by  $\mu = \mu_*/\sigma L^2$ , the ratio of the tidal period and the diffusive time scale.

When the original equations as given in for example [27, 26, 8] are made dimensionless, a parameter  $\epsilon$ , the Strouhal number is found. It is defined by

$$\epsilon = \frac{U}{\sigma L} = \frac{\hat{\zeta}}{H} \quad (2.10)$$

where  $\hat{\zeta}$  is a characteristic amplitude of the free surface variations. This parameter is, apart from a factor of  $2\pi$ , the ratio of the tidal excursion and the tidal inlet length. Since this parameter is small ( $\sim 0.15$  in many estuaries, see table 1), the free surface  $\zeta$ , the velocity profiles, concentration and bottom evolution can be expanded in  $\epsilon$  (see [22]). In the equations used in this paper to describe the hydro- and morphodynamics, only the leading order contributions in  $\epsilon$  are considered. This implies that only diffusive sediment transport is considered.

As an example of an embayment under study, consider the main channel of the Frisian

---

Quantities in the dimensional model		
$H \sim 10 \text{ m}$	$L \sim 2 \cdot 10^4 \text{ m}$	$B \sim 1 - 5 \cdot 10^4 \text{ m}$
$\hat{\zeta} = \frac{HU}{\sigma L} \sim 1.5$	$\gamma \sim 4 \cdot 10^{-3} \text{ s}^{-1}$	$\mu_* \sim 10^2 \text{ m}^2 \text{ s}^{-1}$
$\sigma \sim 1.4 \cdot 10^{-4} \text{ s}^{-1}$	$\alpha \sim 10^{-2} \text{ kg s m}^{-4}$	
Parameters in the non dimensional model		
$\epsilon \sim 0.15$	$a \sim 0.04$	$\mu \sim 1.8 \cdot 10^{-3}$
$\delta_s \sim 8 \cdot 10^{-4}$	$\delta_b \sim 5.4 \cdot 10^{-7}$	

---

TABLE 1. Quantities and parameter values for the Frisian inlet system. The symbols are explained in the text.

---

inlet system [29]. It has an approximate length of 20 km and a depth of 10 m. The forcing is largely due to the  $M_2$  tide with some contribution of the  $M_4$  overtide. The sediment in the channel is fine sand with a grain size of  $2 \cdot 10^{-4}$  m. A typical value for the horizontal diffusion coefficient is  $\mu_* \sim 100 \text{ m}^2 \text{ s}^{-1}$ , as discussed in *e.g.* [18]. Some other useful quantities are listed in the first part of table 1; in the second part of this table, the dimensionless parameters are listed.

### 3. Basic State

As described by (2.8), the system is forced at the entrance of the basin. In this study only the leading order harmonic  $T(t) = \cos t$  is considered (no external overtides) so that  $\zeta = \cos t$  at  $x = 0$ . Using (2.2a) and (2.2b) it is easily seen that

$$\zeta(x, y, t) = \cos t \quad (3.1)$$

which describes a spatially uniform tide in the embayment.

We assume that in equilibrium there is no structure in the  $y$  direction (hence all quantities are independent of  $y$ ) and that the equilibrium velocity in the  $y$  direction is zero. The equations (2.1), (2.5) and (2.6) reduce to

$$-\sin t + [(1 - h_{\text{eq}})u_{\text{eq}}]_x = 0 \quad (3.2a)$$

$$a(C_{\text{eq}t} - \mu C_{\text{eq}xx}) = u_{\text{eq}}^2 - C_{\text{eq}} \quad (3.2b)$$

$$\langle u_{\text{eq}}^2 - C_{\text{eq}} \rangle = 0 \quad (3.2c)$$

where we have used that in equilibrium no bedload transport is present (see section 2). Furthermore, we used that  $\mathbf{F} \sim \mathbf{u}$  (linear friction law), so the vorticity equation (2.2c) is automatically obeyed. A solution of (3.2) is

$$u_{\text{eq}} = -\sin t, \quad v_{\text{eq}} = 0 \quad (3.3a)$$

$$C_{\text{eq}} = \frac{1}{2} - \frac{a}{1 + 4a^2} \left[ \frac{1}{2a} \cos 2t + \sin 2t \right], \quad h_{\text{eq}} = x \quad (3.3b)$$

This equilibrium profile represents a constantly sloping bottom with a spatially uniform velocity field. This means that the one dimensional profile  $h_{\text{eq}} = x$  is an equilibrium profile of the two dimensional equations as well. It is not clear whether or not this equilibrium is stable. In [22] it has been shown that without gravitational effects,  $h_{\text{eq}}$  is stable against small, one-dimensional perturbations. They also showed, using numerical experiments that this equilibrium profile is globally stable against one-dimensional perturbations.

Here we will focus on the stability properties of the basic state with respect to two dimensional perturbations.

In performing the linear stability analysis, no perturbations in the sea level  $\zeta$  are taken into account, because by expanding in  $\epsilon$  it is consistent to neglect these perturbations. Using the boundary condition (2.8) it follows that  $\zeta$  is independent of the lateral coordinate. The lateral momentum equation in which the assumption of a short embayment is not used, but in which terms of order  $\epsilon$  are neglected, reads after scaling (see [27, 22])

$$v_t + \lambda_L^{-2} \zeta_y = F_2^b$$

with  $\lambda_L = L/L_g \ll 1$  and  $F_2^b \sim v$ . From this equation it is clear that at the entrance of the basin  $v = 0$ . Thus by prescribing an excursion of the sea level  $\zeta$  at the entrance of the embayment independent of the coordinate in the lateral direction, no lateral velocity  $v$  is found there.

#### 4. Two-Dimensional Perturbations

In this section, the stability properties of the equilibrium as given in section 3 will be considered with respect to perturbations that can vary in both the  $x$ - and  $y$ -direction. As discussed in section 3, the free surface elevation will not be perturbed. Thus in the equations of motion the following expressions are substituted:

$$\Phi = \Phi_{\text{eq}} + \Phi' \quad (4.1)$$

where  $\Phi = (\zeta, u, v, C, h)^T$  is the solution vector,  $\zeta' = 0$  and  $\Phi_{\text{eq}}$  as given in (3.2). In (4.1), the superscript  $'$  labels the perturbations which are considered to be small with respect to the basic variable. Next, the continuity equation (2.1) and the vorticity equation (2.2c) are linearized with respect to these perturbations. This results in

$$[(1-x)u' + h' \sin t]_x + (1-x)v'_y = 0 \quad (4.2a)$$

$$v'_{tx} - u'_{ty} = -\tilde{F}_{2x}^b + \tilde{F}_{1y}^b \quad (4.2b)$$

where  $\tilde{\mathbf{F}}^b$  is the linearized bottom stress vector (2.4) where only the first term in the Taylor expansion is used. The corresponding boundary conditions can be derived from (2.7)–(2.8) and read

$$(1-x)u' + h' \sin t = 0 \quad \text{at } x = 1 \quad (4.2a)$$

$$v' = 0 \quad \text{at } y = 0, y = \frac{B}{L}, x = 0 \quad (4.2b)$$

The latter condition was discussed in section 3. Thus (4.2)–(4.2) govern the dynamics of the flow perturbations for a given bottom disturbance. Next the sediment transport and sediment balance are considered. In the concentration equation, only the contribution of the concentration that does not average out in the bottom evolution equation has to be calculated. From now on, this contribution is denoted by  $\mathcal{C}'$ . The equation that describes the non-fluctuating part of the concentration reads after linearization

$$-\delta^2 \mathcal{C}'_{xx} - \delta^2 \mathcal{C}'_{yy} = -\langle 2u' \sin t \rangle - \mathcal{C}' \quad (4.3)$$

where  $\delta = \sqrt{a\mu} = \sqrt{\mu_*/\gamma}/L$  is the ratio of the diffusive length scale and the basin length. Linearizing the bottom evolution equation gives

$$h'_\tau = \langle 2u' \sin t \rangle + \mathcal{C}' + \lambda \nabla^2 h' \quad (4.4)$$

The boundary conditions are

$$\langle 2u' \sin t \rangle + \mathcal{C}' = 0, \quad h'_\tau = 0 \quad \text{at } x = 0 \quad (4.5a)$$

$$\frac{h'}{1-x} \text{ finite}, \quad \mathcal{C}'_x + \lambda h'_x = 0 \quad \text{at } x = 1 \quad (4.5b)$$

$$\delta^2 \mathcal{C}'_y = 0, \quad \lambda h'_y = 0 \quad \text{at } y = 0, y = \frac{B}{L} \quad (4.5c)$$

The boundary conditions at the landward side of the embayment ( $x = 1$ ) require some explanation. They are due to the fact that the undisturbed water depth described by the basic state becomes zero at this position. Since we require bounded solutions in this weakly singular point, the first condition follows directly from (4.2a) by requiring that  $u'$  must be finite at  $x = 1$ . Furthermore, at this point no distinction can be made between suspended and bedload transport. Consequently, the total load transport has to vanish.

Now the structure of the equations (4.2a), (4.2b), (4.3) and (4.4) and the boundary conditions on the fixed walls imply that the solutions can be written as

$$u' = \sum_{n=0}^{\infty} [u_n^c(x) \cos t + u_n^s(x) \sin t] \cos(l_n y) \quad (4.6a)$$

$$v' = \sum_{n=0}^{\infty} [v_n^c(x) \cos t + v_n^s(x) \sin t] \sin(l_n y) \quad (4.6b)$$

$$\mathcal{C}' = \sum_{n=0}^{\infty} C_n(x) \cos(l_n y) \quad (4.6c)$$

$$h' = \sum_{n=0}^{\infty} h_n(x) \cos(l_n y) \quad (4.6d)$$

with  $l_n = n\pi L/B$  and  $n = 0, 1, 2, \dots$ . Thus, the lateral spatial structure of the state variables can be expanded in Fourier modes with wavenumber  $l_n$ .

Whenever  $\alpha \neq 0$  in the friction vector (2.4), the frictional terms couple the  $\sin t$  and  $\cos t$  components (see 4.6) of the perturbed velocity field  $\mathbf{u}'$ . Hence one finds phase shifts in time between velocity components, which can result in net sediment transport from troughs to crests of bedforms and hence positive growth rates of the perturbations.

Using (4.2a), (4.2b) and (4.6), the linearized continuity equation reads

$$[(1-x)u_n^s]_x + h_{nx} + l_n(1-x)v_n^s = 0 \quad (4.7a)$$

$$[(1-x)u_n^c]_x + l_n(1-x)v_n^c = 0 \quad (4.7b)$$

and the vorticity equation is given by

$$v_{nx}^s + l_n u_n^s + r l_n [1 + \alpha x] u_n^c + r [1 + \alpha x] v_{nx}^c + \alpha r v_n^c = 0 \quad (4.8a)$$

$$v_{nx}^c + l_n u_n^c + \alpha r l_n h_n - r l_n [1 + \alpha x] u_n^s - r [1 + \alpha x] v_{nx}^s - \alpha r v_n^s = 0 \quad (4.8b)$$

with boundary conditions which can be derived from (4.2).

Using the expansion (4.6), the concentration equation becomes

$$\delta^2 C_{nxx} - (1 + \delta^2 l_n^2) C_n = u_n^s \quad (4.9)$$

and the bottom evolution equation reads

$$h_{n\tau} = (u_n^s + C_n) + \lambda (h_{nxx} - l_n^2 h_n) \quad (4.10)$$

with the boundary conditions to be derived from (4.5a) and (4.5b).

Solutions of this system of equations are of the form

$$\Psi' = \text{Re} \{ (u_n^s, u_n^c, v_n^s, v_n^c, C_n, h_n) e^{\omega\tau} \}$$

with  $\omega$  a complex frequency.  $\text{Re}[\omega]$  is the exponential growth rate,  $\text{Im}[\omega]$  the frequency. Substitute this in (4.7), (4.8), (4.9) and (4.10) and discretize these equations using finite difference techniques (in this paper, central differences were used). Introduce  $\Psi = (\Psi'_1, \Psi'_2, \dots, \Psi'_N)$  where  $\Psi'_i$  is  $\Psi'$  evaluated at grid point  $i$ . This gives a  $6N \times 6N$  matrix  $A(\delta, r, \alpha, l_n, \lambda)$ . Next, a  $6N \times 6N$  matrix  $B$  is defined that is zero everywhere, except at the rows that describe the bottom evolution: in these rows the diagonal element equals one. Now the eigenvalue problem can be written as

$$A\Psi = \omega B\Psi$$

The solutions of this eigenvalue problem that can be solved using standard numerical packages, are the eigenfunctions  $\Psi'$  and the eigenvalues  $\omega$ . They depend on the parameters  $\delta$ ,  $r$ ,  $\lambda$ ,  $l_n$  and  $\alpha$ . The diffusion coefficient  $\delta$  depends on sediment properties and the basin length, the friction parameter  $r$  on the tidal amplitude, tidal frequency and water depth, the bedslope coefficient  $\lambda$  on sediment properties, the length of the embayment and its width and  $l_n$  on the length and width of the basin. The parameter  $\alpha$  is not a real physical parameter and will be chosen either 0 or 1. The stability of the system with different parameter settings will be studied in the next sections. However, one has to be careful in changing the parameters: if one would only change, for example, the diffusion coefficient  $\delta$  by changing the sediment properties, the parameter  $\lambda$  and the long time scale  $\tau$  must be changed as well. Therefore, it is difficult to compare results when only  $\delta$  is changed and the time scale and the bedslope coefficients are kept fixed. However, the width  $B$  only enters the parameter  $l_n$  and a different tidal velocity results in a different friction parameter  $r$ . So in subsequent sections, the stability of perturbations is studied for different basin widths by varying  $l_n$  (keeping  $L$  fixed) and for different tidal velocities by varying  $r$ . Some remarks will be made on the influence of the diffusion coefficient  $\delta$  and the bedslope parameter  $\lambda$  on the stability as well.

In the irrotational case ( $\alpha = 0$ ), an integro-differential equation in  $h$  can be derived. We solved this equation as well to check the more general procedure as described above.

## 5. Potential Flows and Related Bottom Profiles

In this section we will consider a vorticity-conserving velocity field, *i.e.*  $\alpha = 0$  in (4.8). It serves as an illustrative and transparent example of the strength of this method and has the advantage that analytical solutions for flow and concentration field can be found which is not possible anymore in case  $\alpha \neq 0$ . The one dimensional results as discussed in [22] will be checked and extended to situations with bedslope correction ( $\lambda \neq 0$ ). Furthermore, the validity of the asymptotic expansion of the concentration  $\mathcal{C}$  as used in [22] will be discussed for larger wavenumbers  $l_n$ . Later, the effect of bottom stresses will be studied.

From (4.7) and (4.8), it is easily seen that  $\{u_n^s, v_n^s\}$  and  $\{u_n^c, v_n^c\}$  decouple. The equations for  $\{u_n^s, v_n^s\}$  read

$$[(1-x)u_n^s + h_n]_x + l_n(1-x)v_n^s = 0 \quad (5.1a)$$

$$v_{nx}^s + l_n u_n^s = 0 \quad (5.1b)$$

and those for  $\{u_n^c, v_n^c\}$  are given by

$$[(1-x)u_n^c]_x + l_n(1-x)v_n^c = 0 \quad (5.2a)$$

$$v_{nx}^c + l_n u_n^c = 0 \quad (5.2b)$$

The equations (5.2) are from a morphodynamical point of view of no interest, because they do not result in net erosion or deposition of sediment in the linearized bottom evolution equation. Therefore, we will concentrate on (5.1), supplemented with (4.9) and (4.10).

In this section, we will derive an eigenvalue problem in  $h$  by expressing  $u_n^s, v_n^s, C$  in terms of  $h$ . First, the hydrodynamical part of the equations will be solved. A differential equation for  $v_n^s$  is derived by substituting (5.1b) in (5.1a). The resulting equation reads

$$v_{nxx}^s - \frac{v_{nx}^s}{1-x} - l_n^2 v_n^s = l_n \frac{h_{nx}}{1-x} \quad (5.3)$$

Equation (5.3) is recognized as an inhomogeneous Bessel differential equation [1]. Note that the width over depth ratio is still present in the equations, namely in the parameter  $l_n$ .

The solution can be found by e.g. the variation of constant method and reads

$$v_n^s = \left[ A_n I_0[l_n \xi] + B_n K_0[l_n \xi] + l_n K_0[l_n \xi] \int_0^\xi I_0(l_n w) h_{nw} dw \right. \\ \left. - l_n I_0[l_n \xi] \int_0^\xi K_0(l_n w) h_{nw} dw \right] \quad (5.4)$$

Using (5.1b), the profile in the  $x$  direction of the longitudinal velocity reads

$$u_n^s = l_n \left[ A_n I_1[l_n \xi] - B_n K_1[l_n \xi] - l_n K_1[l_n \xi] \int_0^\xi I_0(l_n w) h_{nw} dw \right. \\ \left. - l_n I_1[l_n \xi] \int_0^\xi K_0(l_n w) h_{nw} dw \right] \quad (5.5)$$

with  $I_{0,1}$  and  $K_{0,1}$  the first and second order modified Bessel functions of index 0, 1 respectively (see [1]) and  $\xi = 1 - x$ .

We still have to find the constants  $A_n$  and  $B_n$  using the boundary condition (4.2a) and (4.2b). Using the boundary condition on  $u$  (4.2a) and the regularity condition (4.5b), we find that

$$B_n = h_n|_{\xi=0} = 0$$

Using (4.2b), we find that  $A_n$  is given by

$$A_n = -l_n \frac{K_0(l_n)}{I_0(l_n)} \int_0^1 I_0(l_n w) h_{nw} dw + l_n \int_0^1 K_0(l_n w) h_{nw} dw \quad (5.6)$$

Now consider the concentration equation (4.9) with its boundary conditions. This equation can be solved using the variation of constant method. Introduce

$$\beta = \frac{\delta}{\sqrt{1 + \delta^2 l_n^2}}$$

The complete solution reads

$$C_n = Ae^{-\frac{\xi}{\beta}} + Be^{-\frac{1-\xi}{\beta}} - \frac{\beta}{2\delta^2} \int_0^1 e^{-\frac{k\xi-z}{\beta}} u_n^s dz$$

Using the boundary conditions, the following expressions for  $A$  and  $B$  are found

$$B = \frac{e^{-\frac{1}{\beta}} \left[ \lambda h_\xi(\xi = 0) - \frac{\beta}{\delta^2} \int_0^1 \sinh\left(\frac{z}{\beta}\right) u_n^s dz \right] - u_n^s(\xi = 1)}{1 + e^{-\frac{2}{\beta}}} \quad (5.7)$$

$$A = Be^{-\frac{1}{\beta}} + \lambda h_\xi(\xi = 0) - \frac{\beta}{2\delta^2} \int_0^1 e^{-\frac{z}{\beta}} u_n^s dz \quad (5.8)$$

Using the expressions for  $u_n^s$  and  $C_n$ , we can solve the bottom evolution equation

$$h_{n\tau} = (u_n^s + C_n) + \lambda (h_{n\xi\xi} - l_n^2 h_n) \quad (5.9)$$

Note that the equation for  $h_n$  is an integro-differential equation. We cannot solve this equation analytically anymore. Therefore, numerical tools are used. The problem is solved numerically by using the method of finite differences. Write  $\mathbf{h} = (h_1^*, \dots, h_N^*)e^{\omega\tau}$  where  $h_i^*$  is the value of  $h_n$  at grid point  $i$ . Discretize the integral expression  $C_0$  as  $C_i^* = \sum_j C(i, j)h_j^*$  with  $C(i, j)$  an  $N \times N$  matrix. Now the following eigenvalue problem is obtained

$$\omega \mathbf{h} = \mathcal{L}(x(i), C(i, j), \delta, \lambda) \mathbf{h}$$

This equation can be solved using standard numerical tools. Note that, because the hydrodynamic equations can be solved in closed form, the only unknown variable in the eigenvalue problem the bottom function  $\mathbf{h}$ , whereas in the rotational case all hydrodynamic quantities were found in the eigenvalue problem as well, resulting in a completely different kind of problem (see section 4).

### 5.1. No Gravitational Bedload Effects

In figure 2 the first three eigenvalues which correspond to different longitudinal modes are plotted as functions of the lateral wavenumber  $l_n$  by varying the width of the embayment (see the discussion in section 4). In the numerical experiments, we have chosen  $\delta = 0.01$  and  $\lambda = 0$  which is quite realistic according to table 1. It appears that the eigenvalues are real and negative for all values of the parameter  $l_n$  so that there is no morphodynamic instability mechanism in this case. Note that the parameter  $l_n = n\pi L/B$ . This is, in fact, not a continuous parameter as  $n$  can only take integer values. Hence by fixing the length  $L$  and the width  $B$  of the basin, a discrete number of eigenmodes in the  $y$  direction is obtained, denoted by the integer  $n$ . An example of this is given in figure 2 (Here  $\pi L/B \sim 30$  is chosen, using the parameters for the Frisian inlet system, see table 1). The one dimensional case corresponds to  $n = 0$ . The eigenmodes are characterized by specifying  $l_n$  and the branch at which the eigenvalue lies. In figure 3 the longitudinal structure of first three eigenmodes with  $l_2 = 60$  is plotted. In Figure 4(a) this structure is plotted for different values of  $l_n$  for the first eigenmode (hence the width  $B$  is varied). The same kind of plots are given for the concentration profile in figure 4(b) and the velocities in the  $x$  and  $y$  direction in figures 4(c) and 4(d) respectively. In these figures, all quantities are scaled to 1, in table 2 the maxima of the different physical quantities are given.

We now describe what happens if the parameter  $l_n$  is increased: first of all, we see that the concentration profile and the velocity profile in the  $x$  direction are almost identical, they only have a different sign. This is to be expected for  $\delta l_n \ll 1$  because no large

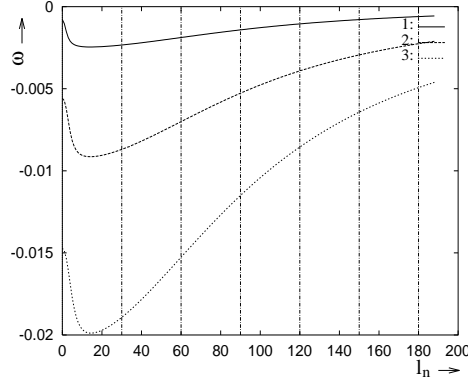


FIGURE 2. Plot of the first three eigenvalues for different values of  $l_n$  with  $\lambda = 0$  and  $\delta = 0.01$ . The vertical lines indicate the values which  $l_n$  can attain in case  $L/B = 30/\pi$ .

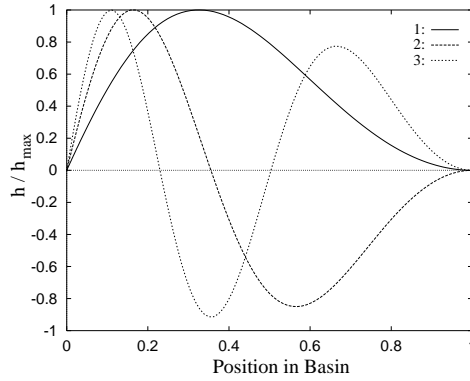


FIGURE 3. First three eigenmodes for  $l_2 = 60$  with  $\lambda = 0$  and  $\delta = 0.01$ .

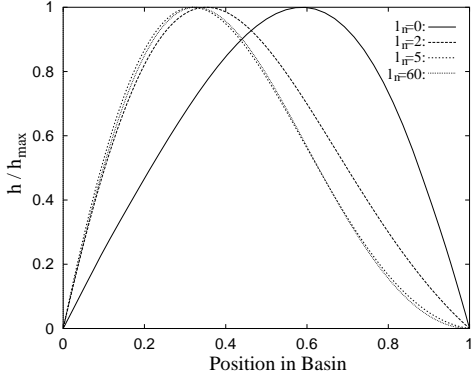
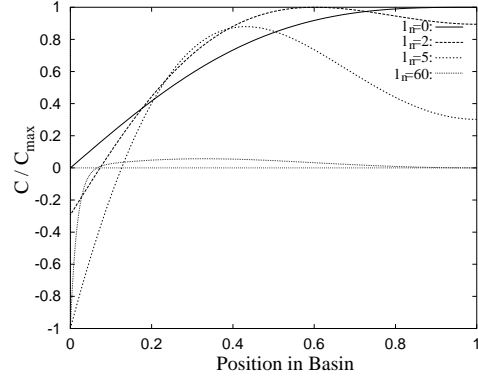
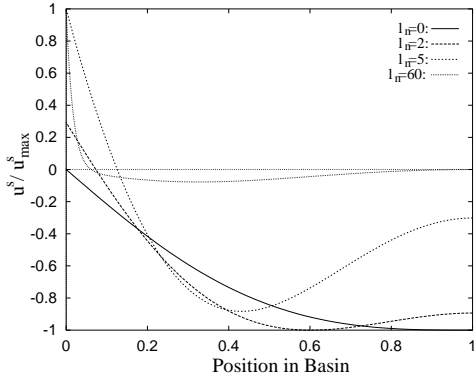
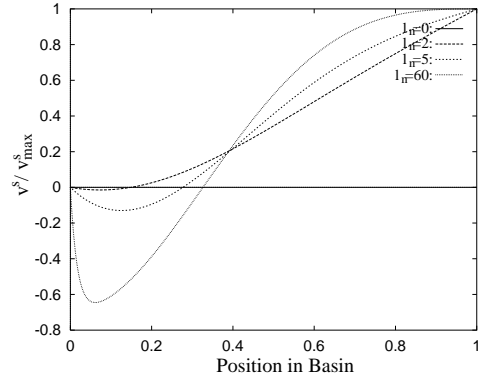
---

wavenumber	$l_n$	$h_{\max}$	$C_{\max}$	$u_{\max}^s$	$v_{\max}^s$
	0	1	2.27	2.27	0
	2	1	1.26	1.27	1.84
	5	1	0.57	0.57	1.29
	60	1	0.09	0.09	0.12

---

TABLE 2. Maxima of the various physical quantities for different values of  $l_n$  (first longitudinal mode).

derivatives in  $C_n$  are encountered (see figure 4(b)) and hence the difference between the perturbed erosion  $u_n^s$  and the perturbed deposition  $C_n$  is of order  $\delta^2$  (see (4.9)). For  $\delta^2 l_n^2 \sim 1$  this is still true, even though a boundary layer near the open end of the basin ( $x = 0$ ) is formed (see figure 4(b)). In the concentration equation the diffusive contribution due to longitudinal gradients is always small: therefore, if  $l_n$  becomes larger (the diffusive term in the lateral direction behaves as  $-l_n^2 \delta^2 C_n$ ) the derivatives in the longitudinal direction become larger as well. From the concentration equation we see that the width of the boundary layer at  $x = 0$  is of  $\mathcal{O}(1/l_n)$ . The last remark we want to make is that the maximum of the velocity  $u_n^s$  and the concentration  $C_n$  is now reached at the seaside of the basin, and not at the closed boundary as in the one-dimensional case. Hence, in increasing the lateral wavenumber  $l_n$  of the perturbation we see that

(a) First eigenmode for the bottom  $h_n$  for different  $l_n$  values(b) First eigenmode for the concentration  $C_n$  for different  $l_n$  values(c) First eigenmode of the velocity  $u_n^s$  for different values of  $l_n$ (d) First eigenmode of the velocity  $v_n^s$  for different  $l_n$  valuesFIGURE 4. Plot of the eigenfunctions for  $\delta = 0.01$  and  $\lambda = 0$ . The irrotational case.

the maxima of  $u_n^s$  and  $C_n$  shift from the landward to the seaside boundary and in this shifting, the bottom perturbation becomes smaller near the landward boundary. For even larger values of  $l_n$  the perturbations will become very small at the seaside and become more pronounced near the landside. However, since these modes are all very stable, they are not of interest in the present analysis.

At this point, we want to emphasize that the asymptotic expansion for  $C_n$  in the small parameter  $\delta$  as used in [22] is not correct: in expanding the concentration  $C_n$ , one assumes that all derivatives of the resulting eigenfunctions are of order one. This assumption is correct for  $\delta l_n \ll 1$  but is violated for larger  $l_n$ . The results obtained by using the asymptotic expansion of the complete solution differ considerably: in the case of the asymptotic expansion, the eigenvalues become complex (see figure 5) and the eigenfunctions become unstable. The eigenfunctions obtained using the asymptotic method become very spiked near the entrance of the basin (see figure 6(b)), thus violating the assumption underlying the asymptotic expansion. Therefore one must be very

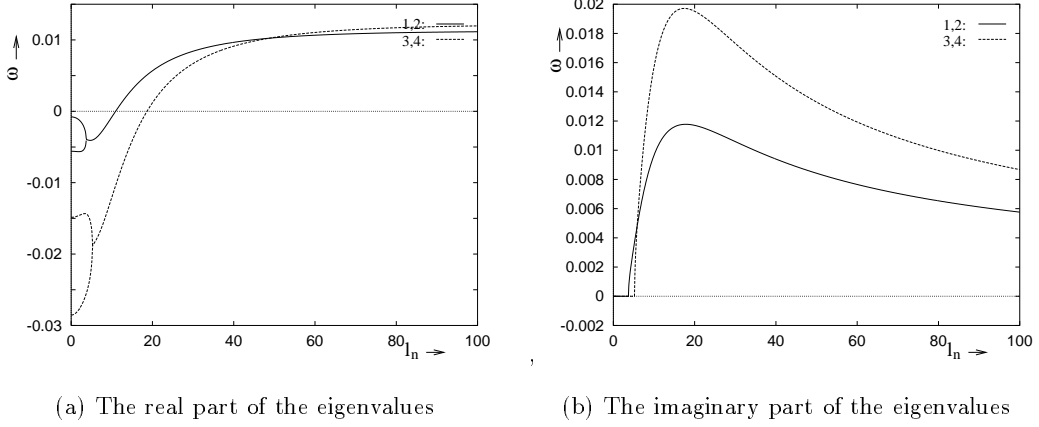


FIGURE 5. The spectrum using the incorrect asymptotic expansion of  $\mathcal{C}$  with  $\delta = 0.1$  and  $\lambda = 0$  (irrotational case). The symbols 1, 2, 3 and 4 refer to the first, second, third and fourth longitudinal mode, respectively. Note that the eigenvalues of branches (1, 2) and (3, 4) become complex conjugates as  $l_n$  passes a critical value.

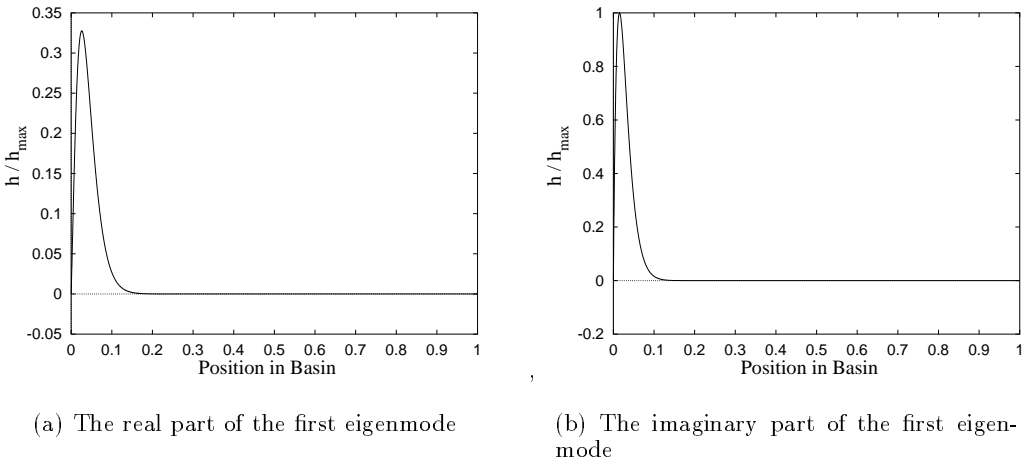
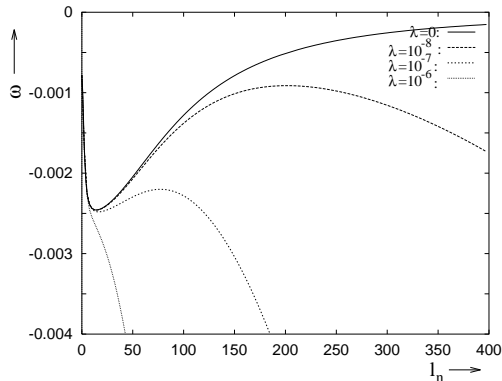


FIGURE 6. The first eigenmode for  $l_n = 60$  using the incorrect asymptotic expansion of  $\mathcal{C}$  with  $\delta = 0.1$  and  $\lambda = 0$ . Note that the eigenfunctions become very spiked near the entrance of the basin in the case of an asymptotic expansion in  $\mathcal{C}$ .

careful in making an asymptotic expansion in the concentration equation in case of two dimensional perturbations.

Note that there is a problem with the results obtained by solving the complete concentration equation as well: from figure 2 it is clear that the fast oscillating modes (*i.e.* with large mode number  $n$ ) become marginally stable (see also Appendix A.1) which is inconsistent with the model assumptions (*i.e.* the use of the shallow water equations). These modes correspond to eigenmodes with large derivatives in the  $y$  direction. In this case, one would expect the sediment to roll down. This effect is modeled by taking  $\lambda \neq 0$ .

FIGURE 7. The first eigenvalue for different values of  $\lambda$ .

### 5.2. Bedload Transport Incorporated

In this section the bedload diffusion parameter  $\lambda$  is made nonzero. It is seen (figure 7) that for large values of  $l_n$  the eigenvalues of the bottom perturbation becomes more and more negative and hence the basic state becomes more stable with respect to these perturbations. This is exactly what we would expect: as  $l_n$  becomes larger, the results from Appendix A.1 with  $\lambda \neq 0$  must be obtained.

### 5.3. One-Dimensional Perturbations

In this section the velocity and bottom profile are chosen independent of  $y$ . This corresponds to the one dimensional case as discussed in [22]. It is of interest to compare the results as presented therein with the results from the two dimensional analysis and to see what the influence of the bedload parameter  $\lambda$  on the results is.

So taking  $n = 0$  in (4.6), it follows from (4.2a) that  $v_0^s = 0$  and that

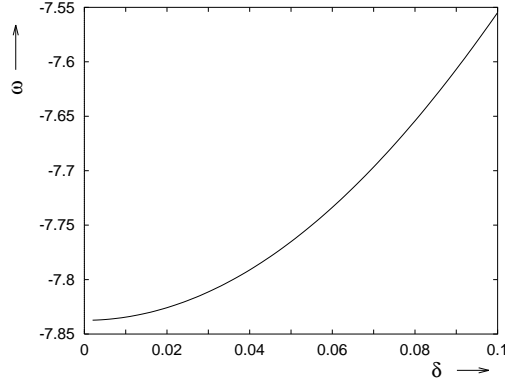
$$u_0^s = -\frac{h_0}{1-x} \quad (5.10)$$

An approximate solution for the concentration  $C_0$  in (4.3) can be found making an asymptotic expansion in the small parameter  $\delta$ . Keeping only the leading order contributions, the bottom evolution equation reads

$$h_{0\hat{\tau}} = \left( \frac{h_0}{1-x} \right)_{xx} + \frac{\lambda}{\delta^2} h_{xx} \quad (5.11)$$

with  $\hat{\tau} = \delta^2 \tau$ .

We expect that the smaller we choose  $\delta$ , the better the approximation  $C_0 = -u_0^s$  will be. First the results without bedload ( $\lambda = 0$ ) will be discussed and a comparison with the results of [22] will be made. In figure 8 the first eigenvalue is plotted as a function of  $\delta$ . The next eigenvalues are smaller than this one for all values of  $\delta$ . Remember that the dimensionless growth rate is defined with respect to the slow time coordinate  $\hat{\tau}$  and hence that as  $\delta \rightarrow 0$  the unscaled growth rate becomes zero. Indeed, if  $\delta = 0$  no bottom evolution can occur since in that case  $h_{0\tau} = 0$ . It is seen that for  $\delta \ll 1$  the results as found in [22] are recovered and that for larger  $\delta$  the eigenvalues change with a rate of  $\mathcal{O}(\delta)$ . In figure 9(a) the first eigenfunction is plotted for different values of  $\delta$  (hence for situations with different turbulence), for  $\delta < 0.01$  the eigenfunctions do not differ significantly from the one with  $\delta = 0.01$ . Values of  $\delta > 0.1$  are not plotted since they are physically not realistic. In figure 9(b) the first three eigenfunctions are

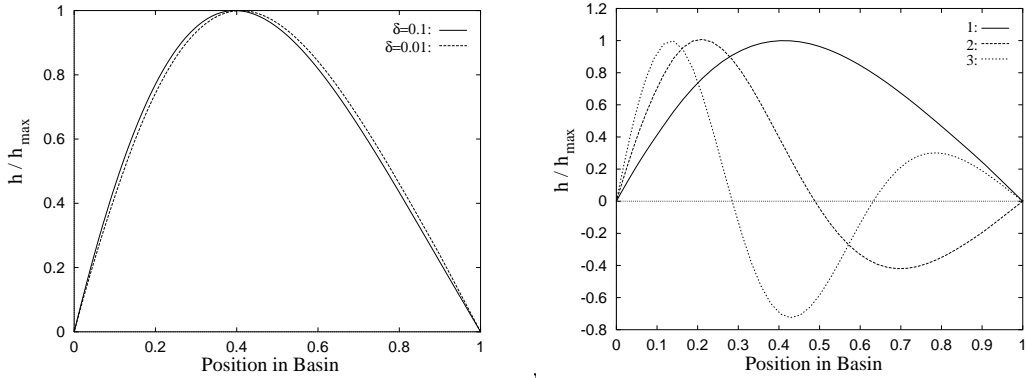
FIGURE 8. The first eigenvalue as a function of  $\delta$  with  $\lambda = 0$ .

---

wavenumber	$h_{\max}$	$C_{\max}$	$u_{\max}^s$
1	1	2.27	2.27
2	1	1.82	1.82
3	1	1.81	1.82

---

TABLE 3. Maxima of the various physical quantities for the first three modes in the longitudinal direction.

(a) First eigenmode for different values of  $\delta$  and  $\lambda = 0$ (b) First three eigenmodes for  $\delta = 0.01$  and  $\lambda = 0$ FIGURE 9. Bottom profiles with  $l_n = 0$ .

plotted for  $\delta = 0.01$ . In figure 10(a) the corresponding velocity profiles are plotted, in figure 10(b) the concentration profiles are shown. In table 3 the maxima of the various physical quantities are given. Here the bottom profiles are all scaled equal to 1.

In figure 11(a) the parameter  $\delta$  is kept fixed at  $\delta = 0.01$  and  $\lambda$  is varied. It is seen that for  $\lambda \rightarrow 0$  the result with  $\lambda = 0$  is retained. It appears that the effect of the bedload term is a stabilizing one, as one would expect from the diffusive character of this contribution. The first eigenmode is plotted in figure 11(b) for different values of  $\lambda$ .

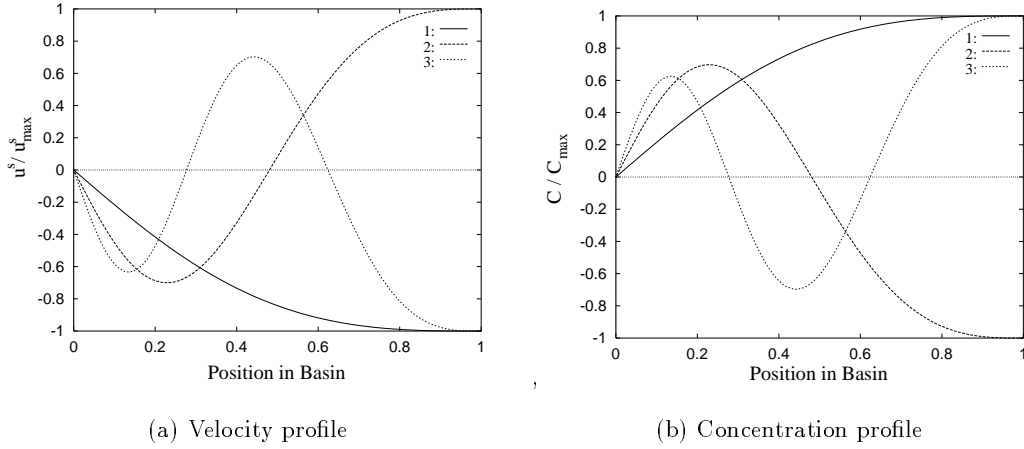


FIGURE 10. Velocity and concentration profiles for  $\delta = 0.01$  and  $\lambda = 0$ . The symbols 1, 2 and 3 refer to the first, second and third longitudinal mode respectively.

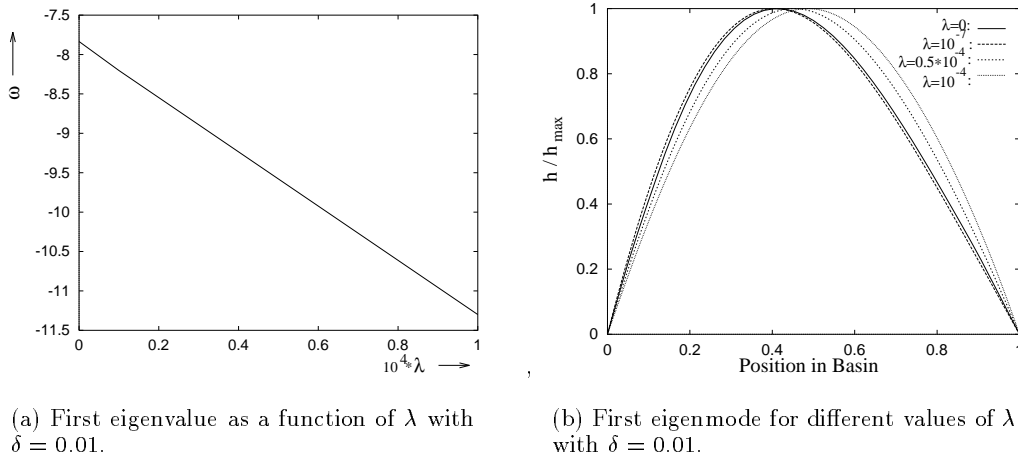


FIGURE 11. Results for different values of  $\lambda$  with  $\delta = 0.01$ .

#### 5.4. Physical Interpretation

In the case of potential flows no perturbations of the basic state with positive growth rate were found. To understand the stabilizing mechanism, the bottom evolution equation is rewritten with the use of the concentration equation, as

$$h'_\tau = -\nabla \cdot \mathbf{F} \quad (5.12)$$

where  $\mathbf{F} = (F_1, F_2)$  is the perturbed total load sediment flux with components

$$F_1 = -\delta^2 \langle C' \rangle_x - \lambda h'_x, \quad F_2 = -\delta^2 \langle C' \rangle_y - \lambda h'_y \quad (5.13)$$

The general condition for instability is that there is a net transport from the trough regions (where  $h' < 0$ ) to the crest regions ( $h' > 0$ ). In the present diffusive model this requires larger concentrations in the trough regions with respect to those in the crest regions. The resulting net convergence (divergence) of the diffusive suspended load flux

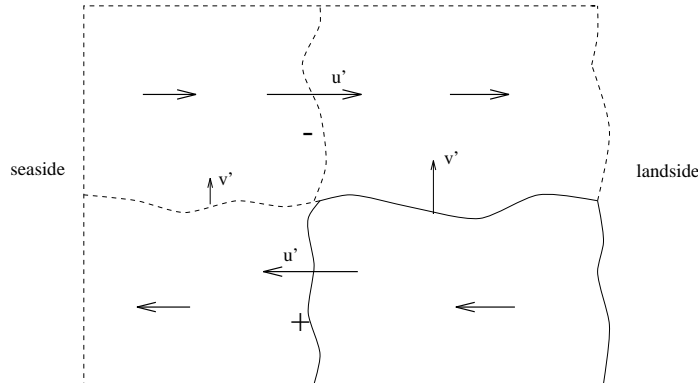


FIGURE 12. Situation sketch of necessary situation for instability during flood. The arrows indicate the direction and magnitude of the perturbed velocities  $u'$  and  $v'$ . The bottom perturbation is positive at the plus sign and negative at the minus sign. For a more complete discussion, see the text.

in the crest (trough) region should be large enough to overcome the stabilizing effects of the slope terms in the total load flux.

Since, to a good approximation,  $C' \sim \langle 2u_0u' \rangle$  (or  $C_n \sim -u_n$ , see figure 5.1 and the discussion in section 5.1), this implies that erosion must be large in the troughs and small in the crests. Consequently, the longitudinal velocity component  $u = u_0 + u'$  must decrease if the tidal flow moves upslope and increase if the flow moves downslope.

In case the flow was irrotational, as was studied in this section, instability behavior is not to be expected because the only tide-topography interaction mechanism is due to continuity effects (*i.e.*, mass conservation) which requires the tidal flow to increase when moving upslope. This can be easily seen in case of the one-dimensional model: the perturbed longitudinal velocity component is given by equation (5.10) and describes a high erosion rate at the crests and low erosion rates in the troughs. Thus there can be no instability.

This statement also holds in case the perturbations are two dimensional and the flow irrotational. Consider for this purpose the situation in figure 12 which shows the distribution of the perturbed longitudinal velocity component, required for unstable behavior near the entrance of the embayment during flood. The ebb-situation follows by reversing all signs. For convenience a bar is selected near  $y = 0$ . It appears that in the region under study  $\partial u'/\partial y$  must be positive. For irrotational flows, this implies positive  $\partial v'/\partial x$  and (since  $v' = 0$  at the entrance) also  $v' > 0$ . Now consider only the downslope area (which is region inside the solid line in figure 12) which is bounded by  $y = 0$ , a line  $y > 0$  where  $u' = 0$  (or, if such a line does not exist, the line  $y = B/L$  is chosen), a line that indicates where  $h_x = 0$  and the right boundary is given by the condition that  $u' = 0$  (which can always be found). At the lower boundary the water flux is zero since  $v' = 0$  here and at the upper boundary there is an outgoing water flux. At the left boundary  $u' < 0$ , implying that  $(1 - x)u' < 0$ , and  $h' > 0$  which means that  $-u_0h' < 0$ . Hence at this boundary there is an outgoing flux since  $\partial v'/\partial x > 0$  and  $v' > 0$ . At the right boundary  $u' = 0$  and  $h' = 0$  which means that no water flux is found through this boundary. Collecting all flux contributions, it is clear that there is a net water flux out of the area under study. Thus in this area, mass conservation is violated, which means that the assumption about distribution of the perturbed velocity component  $u'$  must be wrong. Since this velocity distribution was essential to have morphodynamic instabilities, no instabilities can develop.

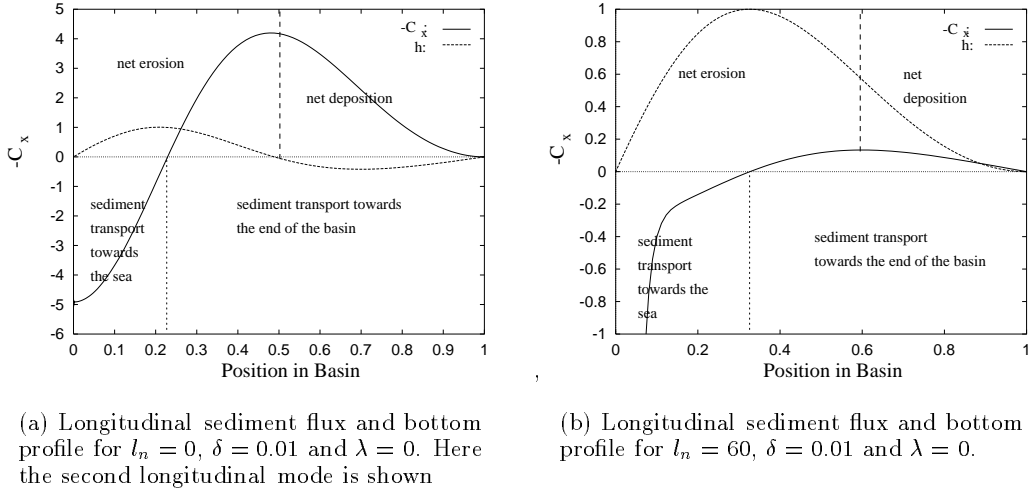


FIGURE 13. Sediment fluxes in the longitudinal direction for  $l_n = 0$  and  $l_n = 60$  with  $\delta = 0.01$  and  $\lambda = 0$ . Here the first longitudinal mode is chosen

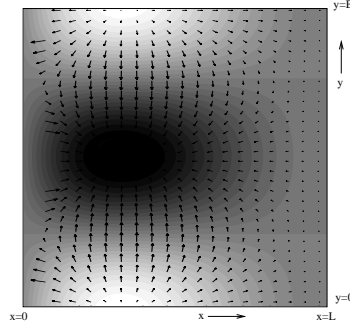


FIGURE 14. Plot of the bottom profile with  $l_n = 60$ ,  $n = 2$ , first longitudinal mode. The crests of the profile are white, the trough is black. The arrows denote the sediment flux. The parameters used were  $\delta = 0.01$ ,  $\lambda = 0$ .

In order to understand and interpret the results obtained so far, let us study the feedback between the tidal flow and the bottom in more detail. In figure 13(a) the sediment flux  $F_x$  for the  $n = 0$  mode is plotted related to the bottom profile denoted by  $h$  in figure 13(a). One observes that there is net erosion at the crests of the bank and net deposition at the troughs. Hence, there is a net diffusive transport from crest to trough, resulting in a negative feedback mechanism. Since there is no variation in the  $y$  direction, no lateral sediment flux is found. In figure 13(b) the sediment flux  $F_1$  for the mode with  $l_n = 60$  is plotted. This flux is related to the bottom profile  $h$  in figure 13(b). Note that at the seaside of the basin the flux becomes very large but remains finite. It is observed that the sediment flux in the  $x$ -direction is not stabilizing throughout the entire basin (as was the case when  $n = 0$ ): at the entrance of the basin, a net erosion due to a flux in the  $x$ -direction is found, at the end of the basin a net deposition occurs. Therefore, the perturbation at the entrance becomes smaller and at the end of the basin larger. However, figure 13(b) only shows the sediment flux in the  $-x$  direction. Since

$l_n \neq 0$ , there is a flux in the lateral direction as well. In figure 14 the total flux is plotted. The sediment flux is in the direction of the arrows, the magnitude of the sediment flux is denoted by the length of the arrows. The fluxes at the entrance are largest (as can be seen from figure 13(b)). Behind the maximum of the bottom profile, it is seen that the sediment is transported from the crests in the direction of the end of the basin, but that the lateral diffusion transports it towards the center of the basin, where the troughs are found. Hence a net sediment flux from crests to trough is found, resulting in a negative feedback mechanism and hence in negative growth rates of the bottom perturbations. Furthermore, note from figures 13(a), 13(b) and 14 that the basin is split into two parts that do not exchange sediment: there is a part near the mouth of the embayment where sediment is imported from and exported towards the sea, then a point in the embayment is found where sediment is only transported in the lateral direction (in the case with  $n = 0$  this means that at this line no convergence or divergence of sediment occurs), and finally well in the embayment the sediment is only redistributed. Hence, away from the entrance of the embayment, the dynamics are not influenced by the possible net import or export of sediment from the sea. Note that for every mode  $n$  the location in the embayment where no longitudinal sediment flux is found differs. Hence only by nonlinear interactions (when no advective contributions are considered) sediment can be imported from the sea towards the end of the embayment.

Using the difference in stability properties of the longitudinal and lateral diffusion, one can get an idea why the perturbations become first more stable if  $l_n$  is increased from  $l_n = 0$  to larger values but after a while get a less negative growth rate: for small  $l_n$  the stabilizing effect of the sediment flux in the lateral direction is stronger than the destabilizing effect of the flux in the longitudinal direction, if  $l_n$  increases more, the destabilizing effect of the sediment flux in the longitudinal direction becomes stronger than the lateral sediment flux. For very large  $l_n$  the results from appendix A.1 can be used. From this it follows that for  $l_n \rightarrow \infty$  the two effects balance each other and hence the growth rate is given by  $\omega = 0$ .

Thus we conclude that in order to have morphologic instabilities, a mechanism should be included which causes a decrease (increase) of the tidal flow while moving in shallower (deeper) water. For irrotational flow this is not possible, but it can occur if the bottom friction terms depend on the water depth. In that case smaller depths induce larger decelerations of the tidal flow over the bars and thus provide for instability conditions. Physically this means that bottom frictional torques are generated and thus vorticity is produced: the flow will no longer be irrotational. This will be the subject of the next session.

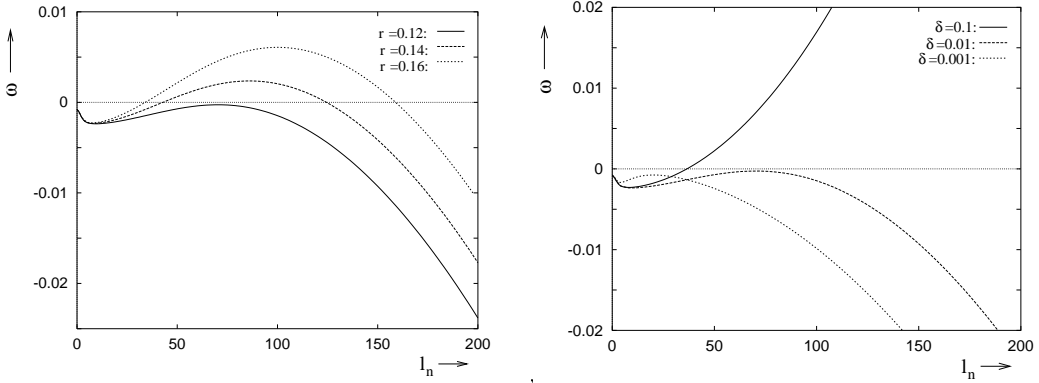
## 6. Frictional Torques

In this section,  $\alpha \neq 0$ . This means that vorticity is not conserved (thus  $\{u_n^s, v_n^s\}$  and  $\{u_n^c, v_n^c\}$  are coupled). If the bedload contribution is neglected ( $\lambda = 0$ ), it can be shown (see appendix A.2) that the bottom perturbations become unstable for large values of  $l_n$ : if  $\alpha \ll 1$ , the growth rate for  $l_n \gg 1$  is given by

$$\omega \approx \frac{\alpha r^2}{1 + r^2} \quad (6.1)$$

Therefore, the gravitational effect will not be neglected in the remainder of this section.

In figure 15(b) the growth rate is shown as a function of the lateral wave number  $l_n$  for various values of the parameter  $r$ , keeping  $\alpha = 1$ ,  $\lambda = 10^{-6}$  and  $\delta = 0.01$  fixed. Furthermore, by varying  $\delta$  and keeping  $r = 0.12$ ,  $\alpha = 1$  and  $\lambda = 10^{-6}$ , it is seen



(a) The first longitudinal eigenvalue for different values of  $r$ ,  $\alpha = 1$ ,  $\lambda = 10^{-6}$  and  $\delta = 0.01$ .

(b) The first longitudinal eigenvalue for different values of  $\delta$ ,  $r = 0.12$ ,  $\alpha = 1$  and  $\lambda = 10^{-6}$ .

FIGURE 15. Eigenvalue plots.

---

wavenumber $l_n$	$h_{\max}$	$C_{\max}$	$u_{\max}^s$	$u_{\max}^c$	$v_{\max}^s$	$v_{\max}^c$
0	1	2.29	2.29	0	0	0
2	1	1.26	1.26	0.04	1.85	0.63
5	1	0.58	0.58	0.09	1.30	0.64
60	1	0.07	0.07	0.13	0.18	0.00

---

TABLE 4. Maxima of the various physical quantities for different values of  $l_n$

(figure 15(b)) that the smaller the grain size, the more unstable the bottom profiles become. In the following pictures, the results of our numerical experiments with  $\delta = 0.01$ ,  $r = 0.14$ ,  $\alpha = 1.0$  and  $\lambda = 10^{-6}$  are shown. In figure 16(a) some bottom profiles are shown. For larger values of  $l_n$  the bottom profiles become more accentuated at the end of the embayment. In figure 16(b) the concentration profile and in figures 17(a)—18(b) the velocity profiles are plotted. Again, in table 3 the maxima of the relevant physical quantities are given.

In case that friction is taken into account, the same behavior as in the frictionless case is observed: a shift of the maximum in the velocity  $u_n^s$  and the concentration profile  $C_n$  from the fixed boundary to the open sea side with increasing mode number (and for even larger mode numbers the concentration of the morphodynamic action at the end of the embayment), the development of a boundary layer near the open sea side for large mode numbers (see section 5.1). Of course, differences can be noted as well. The most important ones are that in the frictionless case, the components of the velocity field that behaved as  $\cos t$  on the short time scale ( $v_n^c$  and  $u_n^c$ ) did not result in morphodynamic changes (see section 5), whereas in the frictional case they have a contribution in the morphodynamic changes by interaction with  $u_n^s$  and  $v_n^s$ . Furthermore, the concentration profile can have a local minimum where the bottom profile exhibits a maximum (see the  $l_n = 60$  mode). Due to the phase shift in time between the velocity components, the maxima and minima of the concentration can be out of phase with the extrema of the bottom perturbations and thus these bottom perturbations can start to grow, depending

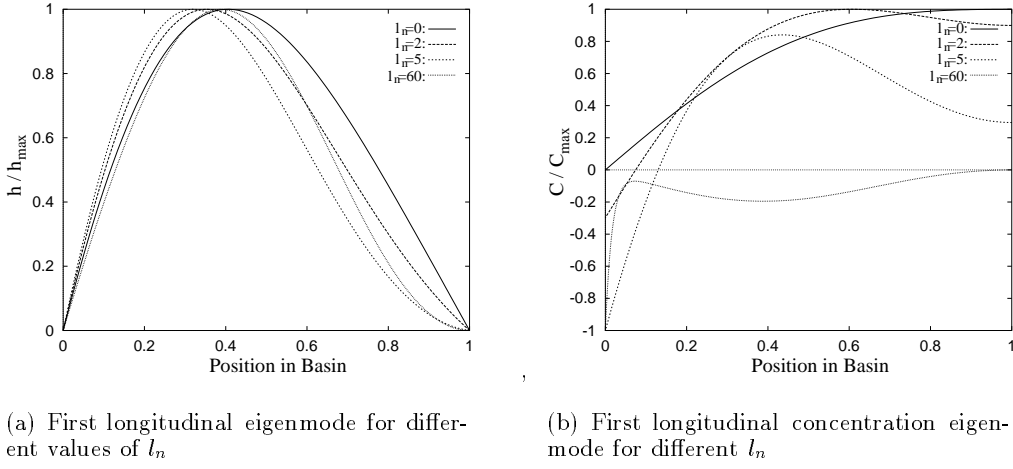


FIGURE 16. Plot of the bottom profiles and concentrations for  $\delta = 0.01$ ,  $\lambda = 10^{-6}$ ,  $\alpha = 1$  and  $r = 0.14$ .

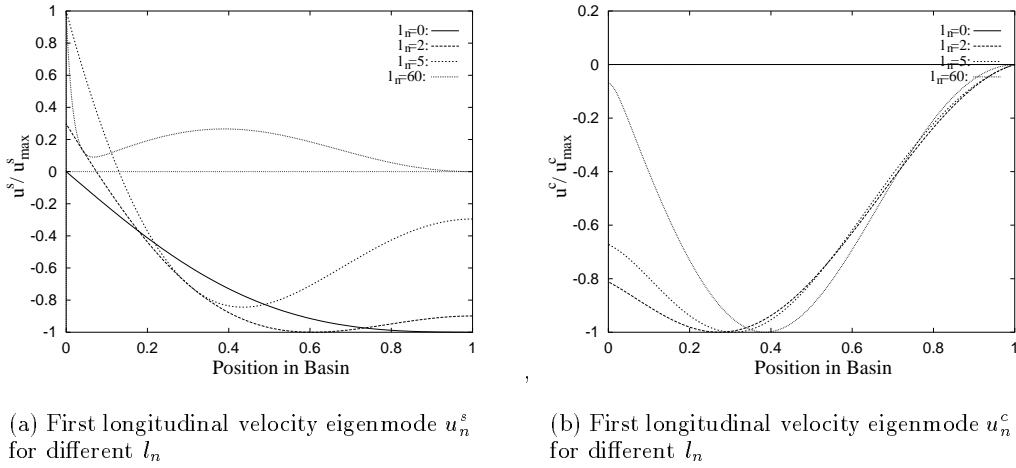


FIGURE 17. Plot of the velocities  $u_n^s$  and  $u_n^c$  in the longitudinal direction for  $\delta = 0.01$ ,  $\lambda = 10^{-6}$ ,  $\alpha = 1$  and  $r = 0.14$ .

on the parameters  $\delta$ ,  $r$ ,  $\lambda$  and  $\alpha$ . If one fixes  $\delta = 0.01$ ,  $\alpha = 1$  and  $\lambda = 10^{-6}$ , a neutral stability curve can be plotted. Here the stability of the first eigenmode in the longitudinal direction is plotted. The other longitudinal modes are always more stable than this one. The control parameter in this plot is the strength of the bottom friction  $r$ . Below a critical value  $r_{cr}$ , all perturbations are damped, above  $r_{cr}$  some of the perturbations have a positive growth rate (see figure 19). Of course, by increasing  $\lambda$  (larger bedload contribution) or by increasing  $\delta$  (larger turbulence induced by small-scale eddies, *e.g.* induced by ripples) these modes can be stabilized. To understand the instability, let us study the mode with  $\alpha = 1$ ,  $r = 0.14$ ,  $\delta = 0.01$ ,  $\lambda = 10^{-6}$  and  $l_n = 60$  with  $n = 2$  (see for example table 1; for the Frisian inlet system, the  $n = 2$  lateral mode would be the first unstable mode). For this mode, the bottom profile and the sediment flux in

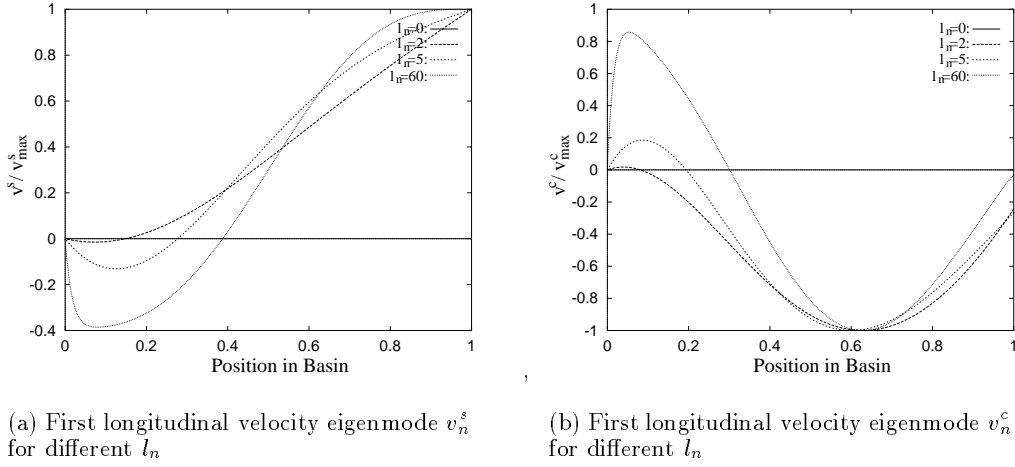


FIGURE 18. Plot of the velocities  $v_n^s$  and  $v_n^c$  in the lateral direction for  $\delta = 0.01$ ,  $\lambda = 10^{-6}$ ,  $\alpha = 1$  and  $r = 0.14$ .

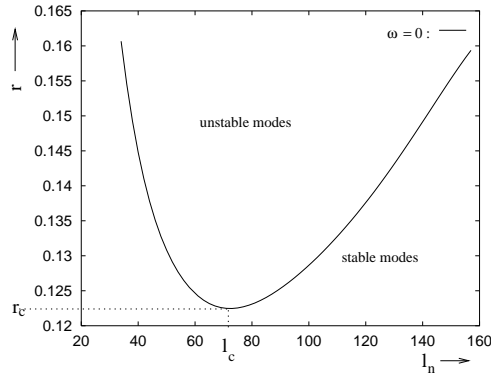


FIGURE 19. Neutral stability curve obtained by varying the friction parameter  $r$ . The parameters used were  $\delta = 0.01$ ,  $\lambda = 10^{-6}$  and  $\alpha = 1$ .

the longitudinal direction are plotted in figure 20. In figure 21 the sediment flux due to the concentration gradients is plotted. The flux due to the bedslope term is always downhill, so it is always stabilizing and hence cannot explain the instability mechanism. One notes that the crest of the perturbation coincides with a convergence of sediment and hence that sediment is moved from the troughs to the crests, resulting in a positive feedback mechanism. Furthermore, it is seen that three regions can be distinguished in the embayment: The first is close to the sea where large fluxes of sediment are coming into the embayment and leave it without penetrating far into the embayment. The second region is observed a little farther into the embayment, where the sediment moves from the "sea-side" to the crests. The last region occurs at the end of the embayment where the sediment moves to the crests coming from the "closed side" of the embayment. Therefore, the large concentration derivatives at the entrance of the embayment do not seem to play a very important role for what happens farther away from the entrance in the basin.

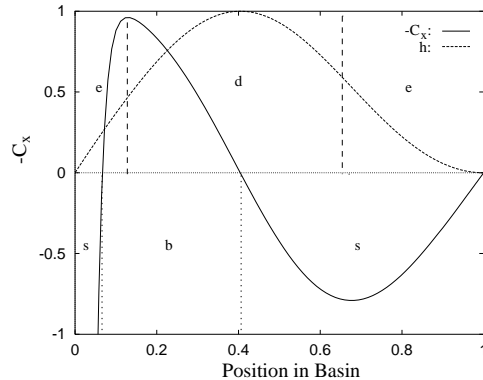


FIGURE 20. Longitudinal sediment flux and bottom profile for  $l_n = 60$ ,  $n = 2$ . The parameters used were  $\delta = 0.01$ ,  $\lambda = 0$ ,  $r = 0.14$  and  $\alpha = 1$ . In this picture "s" stands for sediment moved towards the open sea, "b" for sediment moved into the basin, "e" for regions in the basin where net erosion occurs and "d" those regions where net deposition is found.

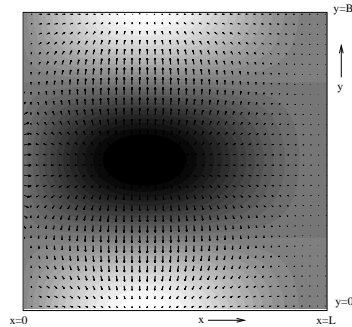


FIGURE 21. Plot of the bottom profile with  $l_n = 60$ ,  $n = 2$ . The crests of the profile are white, the trough is black. The arrows denote the sediment flux. The parameters used were  $\delta = 0.01$ ,  $\lambda = 10^{-6}$ ,  $r = 0.14$  and  $\alpha = 1$ .

## 7. Conclusions

In this paper, we showed that the channel–shoal formation as observed in nature can be explained as a positive feedback mechanism between the tidal flow and the bottom. A necessary condition for instability is the presence of bottom frictional torques. Therefore, no instabilities will be found in an irrotational flow. A necessary condition for the damping of short–scale modes is the introduction of a bedslope term in the total load sediment flux. Now the system becomes selective, *i.e.* a critical lateral wavenumber is found for which the linearly sloping bottom becomes first unstable. The wavenumber depends (among others) on the length  $L$  and width  $B$  of the basin. If the length is kept fixed, a critical width  $B$  is found for which the equilibrium profile becomes unstable for the first time. Which wavenumber is selected depends strongly on the parameter values  $r$  that describes the strength of the friction,  $\delta$  that is related to the grain size and  $\lambda$  which measures the strength of the bedslope term. The most important result is, that if the friction parameter  $r$  is too small, no instabilities occur.

The embayments were considered to be short compared to the tidal wave length and driven by an externally prescribed tide. It was assumed that only the diffusion of sediment in suspension and gravity effects could result in net sediment transport. Since the

tidal time scale is much shorter than the morphodynamical time scale, the method of averaging was used to separate the time scales. The concentration equation was solved exactly since the extension of the approximation as used in [22] (which is correct in the one-dimensional context) to the two-dimensional model gave incorrect results. We studied both a irrotational and a rotational flow. Earth rotating effects were neglected. Due to these assumptions, a comparison can only be made with a small number of embayments, for example the Frisian Inlet. However, the assumptions were only made to keep the analysis transparent and to keep the computational effort to a minimum, since our main interest was to get a better understanding of the basic mechanism that results in instabilities in tidal embayments. The assumptions can be relaxed and more realistic results are to be expected, but even in this simple model it is seen that the system strives for a uniform shear stress. Furthermore, it is observed that after partial closure a net import of sediment takes place. Therefore, this simple model captures much of the necessary physics. The critical mode for the parameters of the Frisian inlet system ( $l_c \sim 60$ ) gives encouraging results since it predicts that the constantly sloping bottom becomes unstable and channels are formed (this is in good agreement with simulations done with the morphodynamic model DELFT2D-MOR). However, the critical friction coefficient ( $r_c \sim 0.125$ ) is too small and a nonlinear theory is necessary to predict possible new equilibrium profiles (under investigation, see [21]).

It appears that the instabilities found are such that length of the basin is split into two or three independent regions. Between these regions, no exchange of sediment is found. Therefore, the large influxes of sediment at the entrance of the embayment (and hence the boundary conditions at the open end) do not play a very important role inside the embayment and hence do not influence the instability mechanism. Exchange of sediment between these different regions will probably occur if advective contributions or nonlinear effects are taken into account.

At this point, only real eigenvalues are found. This means that the bottom profiles will not migrate. However, the migration of bed forms will certainly be observed if nonlinear interactions are taken into account. Probably the introduction of advection in the concentration equation will result in moving bedform as well. The perturbations resemble in some sense the observed channel-shoal systems in tidal embayments: nonlinear interactions of different perturbations will give finite amplitudes of the profiles and might result through a series of bifurcations in a system as observed in nature. Therefore, it is important to extend this linear theory to a nonlinear one to see if the physical mechanism described in this paper can indeed result in the fractal structures of the channels as observed in nature. The results so far are promising and will be discussed in a forthcoming paper. Furthermore, advective processes which were omitted from the concentration equation should be taken into account, because the advective and diffusive processes are usually of the same order of magnitude. It might be that the advective processes stabilize the fast oscillating modes without having to introduce a bedload mechanism. Next, the interaction with the open sea must be understood better to get better boundary conditions at the open end of the embayment.

#### REFERENCES

- [1] M. ABRAMOWITZ AND I. A. STEGUN, *Handbook of mathematical functions*, Dover Publications, New York, 1965.
- [2] D. G. AUBREY AND P. E. SPEER, *A study of nonlinear tidal propagation in shallow inlet/estuarine systems. part 1: Observations*, Est. Coastal Shelf Sci., 21 (1985), pp. 185–205.
- [3] G. T. CSANADY, *Circulation in the coastal ocean*, Reidel, Dordrecht, 1982.

- [4] K. DE JONG AND A. HEEMINK, *A model for long-term morphodynamic behaviour of tidal basins, long estuaries, and tidal rivers*, Tech. Rep. 96-153, Delft University of Technology, 1996.
- [5] H. DE VRIEND AND J. RIBBERINK, *Mathematical modelling of meso-tidal barrier island coasts. part ii: Process-based simulation models*, in *Advances in coastal and ocean engineering*, P.-F. Liu, ed., World Scientific, 1996, pp. 151-197.
- [6] H. J. DE VRIEND, *Mathematical modelling of meso-tidal barrier island coasts. part i: Empirical and semi-empirical models*, in *Advances in coastal and ocean engineering*, P.-F. Liu, ed., World Scientific, 1996, pp. 151-197.
- [7] J. DRONKERS, *Tidal asymmetry and estuarine morphology*, *Neth. J. Res.*, 20 (1986), pp. 117-131.
- [8] K. R. DYER, *Coastal and estuarine sediment dynamics*, John Wiley & Sons, Chichester, 1986.
- [9] K. R. DYER AND R. L. SOULSBY, *Sand transport on the continental shelf*, *Ann. Rev. Fluid Mech.*, 20 (1988), pp. 295-324.
- [10] J. EHLERS, *The Morphodynamics of the Wadden Sea*, Balkema, Rotterdam, 1988.
- [11] A. FALQUES, A. MONTOTO, AND V. IRANZO, *Bed-flow instability of the longshore current*, *Cont. Shelf Res.*, 15 (1996), pp. 1927-1964.
- [12] C. T. FRIEDRICHS, 31 (1988).
- [13] C. T. FRIEDRICHS AND D. G. AUBREY, *Tidal propagation in strongly convergent channels*, *J. Geophys. Res.*, 99 (1994), pp. 3321-3336.
- [14] M. KROL, *On a Galerkin-averaging method for weakly nonlinear wave equations*, *Math. Appl. Sci.*, 11 (1991), pp. 649-664.
- [15] R. McBRIDE, M. BYRNES, AND M. HILAND, *Geomorphic response-type model for barrier coastlines: a regional perspective.*, *Mar. Geol.*, 126 (1995), pp. 143-159.
- [16] A. P. OOST, *Dynamics and sedimentary development of the Dutch Wadden Sea with emphasis on the Frisian Inlet.*, PhD thesis, Utrecht University, 1995.
- [17] B. B. PARKER, ed., *Tidal Hydrodynamics*, New York, 1991, John Wiley & Sons.
- [18] H. RIDDERINKHOF AND J. T. F. ZIMMERMAN, *Chaotic stirring in a tidal system*, *Science*, (1992), pp. 1107-1111.
- [19] J. A. SANDERS AND F. VERHULST, *Averaging methods in nonlinear dynamical systems*, Springer-Verlag, New York, 1985.
- [20] R. SCHIELEN, A. DOELMAN, AND H. E. DE SWART, *On the nonlinear dynamics of free bars in straight channels*, *J. Fluid Mech.*, 252 (1993), pp. 325-356.
- [21] H. SCHUTTELAARS, *Nonlinear, long term equilibrium profiles in a short tidal embayment*, 1997.
- [22] H. SCHUTTELAARS AND H. DE SWART, *An idealized long-term morphodynamic model of a tidal embayment*, *Eur. J. Mech., B/Fluids*, 15 (1996), pp. 55-80.
- [23] G. SEMINARA AND M. TUBINO, *Bed formation in tidal channels: analogy with fluvial bars*, in *Morphology of rivers, estuaries and coasts*, DiSilvio, ed., IAHR Congress, London, contr. II, 1997.
- [24] P. E. SPEER AND D. G. AUBREY, *A study of nonlinear tidal propagation in shallow inlet/estuarine systems. part 2: Theory*, *Est. Coastal Shelf Sci.*, 21 (1985), pp. 207-224.
- [25] A. R. VAN DONGEREN AND H. J. DE VRIEND, *A model of morphological behaviour of tidal basins*, *Coastal Eng.*, 22 (1994), pp. 287-310.
- [26] L. C. VAN RIJN, *Principles of sediment transport in rivers, estuaries and coastal seas*, Acqua Publ., Amsterdam, 1993.
- [27] VREUGDENHIL, *Numerical methods for shallow water flow*, Water Sci. & Techn. Libr., Kluwer, Norwell (MA), 1994.
- [28] Z. WANG, T. LOUTERS, AND H. DE VRIEND, *Morphodynamic modelling for a tidal inlet in the wadden sea*, *Sea. Mar. Geol.*, 126 (1995), pp. 289-300.
- [29] Z. B. WANG, T. LOUTERS, AND H. J. DE VRIEND, *A morphodynamic model for a tidal inlet*, in *Computing Modelling in Ocean Engineering '91*, A. Arcilla and Others, eds., Rotterdam, 1992, Balkema, pp. 235-245.
- [30] J. T. F. ZIMMERMAN, *On the Lorentz linearization of a quadratically damped forced oscillator*, *Phys.Lett.*, 89A (1982), pp. 123-124.
- [31] ———, *On the lorentz linearization of a nonlinearly damped tidal helmholtz oscillator*, *Proc. Kon. Ned. Akad. v. Wetensch.*, 95 (1992), pp. 127-145.

## Appendix A. Asymptotic analysis for large mode numbers

### A.1. The Frictionless Case

In this appendix, it will be shown that for large values of the parameter  $l_n = n\pi L/B$  the eigenvalues of the corresponding eigenmodes tend to go to zero if no bedload transport is incorporated in our model. Large values of  $l_n$  mean  $l_n^2 \delta^2 \gg 1$ . First, combine the continuity equation (4.2a) and vorticity equation (4.2b) and introduce the expansion (4.6) to find the following differential equation for  $u$ :

$$\left[ \frac{1}{1-x} [(1-x)u]_x \right] + l_n^2 u = \left( \frac{h_x}{1-x} \right)_x \quad (\text{A } 1)$$

Near  $x = 0$  and  $x = 1$  the full equations have to be used to describe  $u$ . Away from the boundaries, use that  $l_n^2 \gg 1$  and hence that the first term on the lefthand side of (A 1) is much smaller than the second term. Hence  $u$  can be approximated by

$$u = \frac{1}{l_n^2} \left( \frac{h_x}{1-x} \right)_x \quad (\text{A } 2)$$

Furthermore, using the results obtained numerically and the boundary condition (4.5b), it is easily seen that  $h \rightarrow 0$  as  $x \rightarrow 1$ . Note that our approximation becomes better as  $l_n \rightarrow \infty$ .

The concentration equation is given by

$$C + u = \delta^2 (C_{xx} - l_n^2 C)$$

As an approximation for the concentration for  $l_n^2 \delta^2 \gg 1$ , away from  $z = 0$  and  $z = 1$  where boundary layer corrections must be calculated, we can use

$$C = -\frac{1}{\delta^2 l_n^4} \left( \frac{h_x}{x} \right)_x \quad (\text{A } 3)$$

Combining these results, the bottom evolution equation becomes

$$h_\tau = C + u = \left( \frac{1}{l_n^2} - \frac{1}{\delta^2 l_n^4} \right) \left( \frac{h_x}{(1-x)} \right)_x \quad (\text{A } 4)$$

If we use as boundary conditions that near  $x = 1$  the sediment flux  $-C_x$  is zero and  $h/(1-x)$  must be finite and that near  $x = 0$   $h = 0$ , this equation can be solved in terms of Bessel functions (see [22]). As a first approximation the eigenvalues must satisfy ( $\delta^2 l_n^2 \gg 1$ )

$$J_{\frac{2}{3}} \left( \frac{2}{3} l_n \sqrt{-\omega} \right) = 0$$

with  $J_{2/3}$  the first order Bessel function of index  $2/3$ . If we denote the first zero of  $J_{2/3}(\xi)$  by  $\rho$ , we find that the growth rate  $\omega$  is given by

$$\omega = -\frac{9\rho^2}{4l_n^2} \quad (\text{A } 5)$$

Since  $\rho$  is finite and  $l_n \rightarrow \infty$ , it is clear that  $\omega \rightarrow 0$  as  $l_n \rightarrow \infty$ . Furthermore, we have checked this relation for the first eigenvalue and the numerical results. The results are shown in figure 22. From (A 5) it is seen that  $\omega$  is in leading order independent of  $\delta$ .

Using the asymptotic equation for  $h$ , it is clear that if the gravity term from the bedload transport contribution is retained, this term will always become the largest contribution

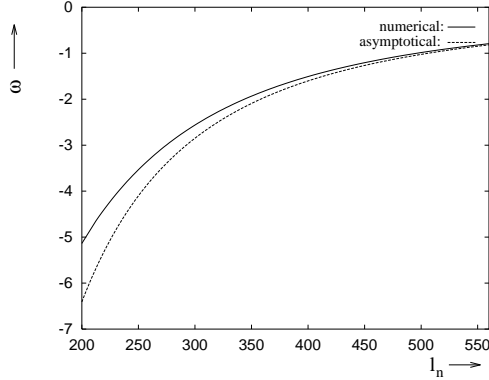


FIGURE 22. Comparison of numerically found eigenvalues and asymptotic eigenvalues for  $\delta = 0.01$ .

for  $l_n \gg 1$ . Indeed, if

$$\frac{1}{l_n^2} \ll \lambda l_n^2$$

the bottom evolution equation reduces to a simple diffusion equation due to the bedload contribution. This equation has the appropriate behaviour for large  $l_n$ , namely that the fast oscillating perturbations will be strongly damped.

#### A.2. Introducing Friction

If friction is introduced, the vorticity equation (4.2b) becomes

$$i v_{nx} + i l_n u_n = r [(1 + \alpha x)] v_{nx} - l_n \left[ -\frac{r\alpha}{2i} h_n + r (1 + \alpha x) u_n \right] \quad (\text{A } 6)$$

Here it is clearer to not split  $u_n$  and  $v_n$  in terms proportional to  $\sin t$  and  $\cos t$  but leave them complex. Thus  $u_n \sim e^{it}$ ,  $v_n \sim e^{it}$  and  $h_n$  real. Outside the boundary layers, we see that for  $l_n \gg 1$  in leading order

$$u_n = \frac{\alpha r}{2i} \frac{1}{i + r[1 + \alpha(1 - z)]} h_n$$

and, using the concentration equation (4.9),

$$C_n = -\frac{1}{a\mu l_n^2} \text{Re}(u_n)$$

If  $l_n \gg 1$  then  $\text{Re}(u_n) \gg C_n$ . Hence the bottom evolution equation becomes

$$h_{n\tau} = \text{Re}(u_n) + \dots$$

If we consider  $\alpha \ll 1$  and write  $h_{n\hat{\tau}} = \omega h_n$ , this equation can easily be solved:

$$\omega \approx \frac{\alpha r^2}{1 + r^2} \quad (\text{A } 8)$$

If  $\alpha \ll 1$  a better approximation has to be made. However, it is clear from the role of  $\alpha$  that if  $\alpha$  increases, the instability mechanism becomes stronger and hence for large  $l_n$  the eigenmodes become more unstable. Thus in case of  $\alpha \ll 1$ , the growth rate tends to a constant for  $l_n \gg 1$ . This means that very fast oscillating modes become unstable unless  $\lambda \neq 0$ . Of course, this analysis is a large simplification of the real equations, because

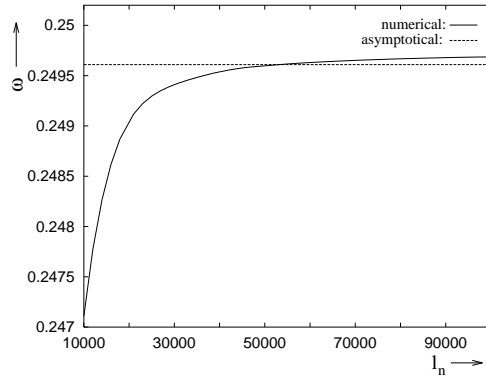


FIGURE 23. Comparison of numerically found eigenvalues and asymptotic eigenvalues with  $\delta = 0.1$ ,  $\alpha = 0.1$  and  $r = 0.16$ .

the differential character is of the equations is lost. Therefore, one expects that the eigenvalues found using the complete equations do not exactly correspond to the value found in this crude analysis. It turns out that at least the order of magnitude and the sign of the eigenvalues is given correctly by the above analysis. A comparison between numerically found eigenvalues and the asymptotic approximation is given in figure 23. Here the situation with  $\delta = 0.1$ ,  $\alpha = 0.1$  and  $r = 0.16$  is considered.

If  $\lambda \neq 0$ , the bottom evolution equation will become diffusively dominated for  $l_n \gg 1$  (see section A.1) and hence the fast oscillating modes will be damped.